

THE ENVIRONMENT AND STRUCTURE OF MASSIVE CENTRAL GALAXIES USING THE SUBARU HYPER SUPRIME-CAM SURVEY

SONG HUANG (黃崧)¹ ALEXIE LEAUTHAUD¹, KEVIN BUNDY¹, MICHAEL STRAUSS², YEN-TING LIN³, RACHEL MANDELBAUM⁴

Draft version -1

ABSTRACT

Although the environmental dependence of structures for massive central galaxies is predicted by the promising hierarchical assembly model, observations at low redshift seem to find no convincing evidence for that. With the help of deep *i*-band images of a large sample of massive central galaxies at $0.3 < z < 0.5$ from the Subaru Hyper Suprime-Cam (HSC) survey, we map their stellar mass distributions out to radius larger than 100 kpc, and discover subtle, but systematic and robust structural differences that depend on halo mass. At fixed stellar mass within 100 kpc, the massive central galaxies in more massive ($M_{200,c} \gtrsim 1.6 \times 10^{14} M_\odot$) halos have a slightly flattened inner profile within $\sim 15\text{--}20$ kpc, and a more prominent outer envelope compared to ones in less massive ($M_{200,c} \gtrsim 8.7 \times 10^{13} M_\odot$) halos. For centrals with $M_* > 10^{11.5} M_\odot$, the ones in more massive halos show very significant excess of mass in the outskirt when the two samples are matched using proxies of mass assembled at $z > 1$. Such differences are broadly consistent with richer recent merging history for more massive halos. We suggest that the relation between total stellar mass and mass within inner 5 or 10 kpc is potentially interesting for diagnosing the role played by host halo in shaping the structures of massive central galaxies. These results also highlight the importance of deep photometry and the usage of detailed structural information in the study of the assembly history of galaxies.

Subject headings: galaxies: elliptical and lenticular, cD — galaxies: formation — galaxies: photometry — galaxies: structure — galaxies: surveys

1. INTRODUCTION

Scientific Background

- Massive galaxies are important cosmic probe and unique labs to study galaxy evolution.
- Briefly explain why massive early-type galaxies are important through the difficulties of stellar-halo mass relation and stellar mass function at the high-mass end.
- Brief summary of the current understanding of their cosmic assembly history.
- Explain why we should care about the environment, and why we expect to see some environmental dependence in the structure and other properties of massive galaxies.
- Brief review of the current observations. It is still not clear whether there is a clear environmental dependence.

Observational difficulties (a.k.a Why we need HSC)

- Explain why it is important to study the mass distribution of massive galaxies out to large physical radius; and, given their unique light profiles, why it is more difficult to study them compared to late-type galaxies.
- Very brief summary of past observational efforts, and why they are not good enough (Not enough number of really massive galaxy; Shallow images; Background subtraction issue; and stacking analysis can be dangerous as while)

Basic idea of this work

- Here we take advantages of the ambitious Hyper-Suprime camera survey...

To achieve this goal, we will select $\log(M_*/M_\odot) > 11.5$ massive central galaxies within host halo mass larger and smaller than $\log(M_{\text{Halo}}/M_\odot) = 14.0$ at $0.3 < z < 0.5$. As both M_* - M_{Halo} relation and stellar mass function are still quite uncertain at $\log(M_*/M_\odot) > 11.5$, it is of great interest to investigate the structure of galaxies in this region carefully. Under the adopted cosmology, $1.0''$ equals 4.4 and 6.1 kpc at redshift 0.3 and 0.5. Therefore, this redshift range enables us to reliable measure the total stellar mass within the inner 5 to 10 kpc (where the “in-situ” component should still dominates) of massive galaxies at the high redshift end assuming the typical seeing of HSC data. At the same time, the depth of the HSC image allows to map the stellar distribution of these galaxies out to ~ 100 kpc at $z \sim 0.5$. Within these stellar mass and redshift range, we can select a large sample of galaxies from the current ~ 100 square degree of HSC data, and safely ignore significant mass growth and structural evolution (no star formation, lower merger rate et al. e.g. Bellstedt et al. 2016, Inagaki et al. 2015; but also see Bai et al. 2014; more discussion about this in Section 5).

The paper is organized as follows. Section 2 gives a brief overview of the HSC observation and data reduction. We will also summarize the process of sample selection. In Section 3, we will describe the method for deriving the stellar mass surface density profile. The main results are summarized in Section 4. Section 5 provides discussions of the assumptions used

¹Kavli Institute for the Physics and Mathematics of the Universe, The University of Tokyo Institutes for Advanced Study, the University of Tokyo (Kavli IPMU, WPI), Kashiwa 277-8583, Japan

²Princeton University Observatory, Peyton Hall, Princeton, NJ 08544, USA

³Institute of Astronomy and Astrophysics, Academia Sinica, P.O. Box 23-141, Taipei 10617, Taiwan

⁴Carnegie-Mellon University **TODO: correct affiliation here**

in this work, the potentially interesting physical implications, and several future improvements, ending with a summary in Section 6.

All the magnitudes used here are in AB system (Oke & Gunn 1983), and are corrected for Galactic extinction using calibrations from Schlafly & Finkbeiner (2011). Within this work, we assume $H_0 = 70 \text{ km s}^{-1} \text{ Mpc}^{-1}$, $\Omega_m = 0.3$, and $\Omega_\lambda = 0.7$.

2. DATA AND SAMPLE SELECTION

2.1. The Hyper Suprime-Cam Survey

The Subaru Strategic Program (SSP, REF) makes use of the new prime-focus camera, the Hyper Suprime-Cam (HSC; Miyazaki et al. 2012), on the 8.2-m Subaru telescope at Mauna Kea. Taking advantage of the large field of view (FoV; 1.5 deg in diameter) of HSC, this ambitious multi-layer photometric survey will cover $\sim 1400 \text{ deg}^2$ of sky in 5 broad bands ($g\ r\ i\ z\ Y$) to the depth of $r \sim 26$ mag in the WIDE part in the next few years. This work is based on the internal data release S15B, which covers ~ 100 square degree of sky in all 5-band to the required depth of WIDE survey. The regions covered by this release are overlapped with several previous spectroscopic survey (e.g. SDSS/BOSS: Eisenstein et al. 2011, Alam et al. 2015; GAMA: Driver et al. 2011, Liske et al. 2015).

The data are processed with `hscPipe` 4.0.1, a derivative of the Large Synoptic Survey Telescope (LSST) pipeline (e.g. Ivezić et al. 2008; Axelrod et al. 2010), modified for use with Suprime-Cam and Hyper Suprime-Cam. `hscPipe` first bias subtract, flat field, model background, and perform object detection and measurement on the single exposure data. Then, different exposures are warped onto a common World Coordinate System (WCS) and combined into final images with improved signal-to-noise ratio (SNR) after astrometric and photometric calibration. The pixel scale of the combined images is $0.168''$. The photometric calibration is based on data obtained from the Panoramic Survey Telescope and Rapid Response System (Pan-STARRS) 1 imaging survey (Schlafly et al. 2012, Tonry et al. 2012, Magnier et al. 2013). To achieve consistent deblending and photometry across all bands, the `hscPipe` will perform multi-band post-processing on the combined images. The footprints and peaks of detected sources on each band will be merged into a single catalog. This consistent set of peaks and footprints is used as starting point for deblend and measure objects on the combined images of each band. These measurements are then merged into a reference catalog. After fixing the centroids, shape, and other non-amplitude parameters of every object in this catalog, `hscPipe` will derive forced photometry measurements at each band. Details of `hscPipe` and the multi-band processing method will be presented in REF (Bosch et al. in prep.).

In Figure 1, we compare the false color (gri) images of nearby massive galaxies from both SDSS and HSC surveys. The RGB images are generated using similar scaling and color schemes, and clearly demonstrate the capability of HSC to map the stellar distribution out to the very outskirt of these massive galaxies, where important fossil records about their recent assembly history are stored. In i -band (ignoring the slight difference in filter response curve), the HSC WIDE image is on average 3.0-4.0 magnitude deeper than SDSS, which gives us significant advantage in studying massive ETGs given their extended, shallow outer surface brightness profiles.

Motivated by the requirement of weak lensing analysis, the i -band data typically has the best seeing in all five bands (the median seeing is around $\text{FWHM} \sim 0.7''$). Therefore, we will mostly use the i -band images to study the structure of galaxies.

2.2. redMaPPer cluster catalog

In order to select the central galaxies from cluster level dark matter halos (e.g. $> 10^{14} M_\odot$), we make use of the redMaPPer cluster catalog⁵ (v5.1.0, e.g. Rykoff et al. 2014; Rozo et al. 2015b). These clusters are selected from the SDSS DR8 photometric data using overdensity of red-sequence galaxies. For each cluster, the catalog provides robust estimations of photometric redshift z_λ and richness λ , along with the best candidate of the central galaxy (the one with the highest central probability P_{CEN}). Information about the identified member candidates is also provided separately. Please see Rozo & Rykoff (2014), Rozo et al. (2015a), Rozo et al. (2015b) for more details about the performance of the redMaPPer cluster catalog. Several works (e.g. Saro et al. 2015; Farahi et al. 2016; Simet et al. 2016) have tried to calibrate the $M_{200,c} - \lambda$ relation using different methods. Despite the slightly different calibrations derived, it is safe to assume that most clusters identified by redMaPPer ($\lambda > 20$) have $\log(M_{200,c}/M_\odot) \geq 14.0$. Considering the typical uncertainty of richness, and the fact that redMaPPer catalog starts to become incomplete toward low richness ($\lambda < 40$) end at $z > 0.33$, we will focus on the $\lambda > 30$ clusters in this work. Based on the calibrations from Farahi et al. (2016) or Simet et al. (2016), such richness cut gives us haloes with $M_{200c} \geq 1.56 \pm 0.35 \times 10^{14} M_\odot$ or $M_{200c} \geq 1.60 \pm 0.11 \times 10^{14} M_\odot$. Therefore, redMaPPer can provide us a sample of massive central galaxies in $\log(M_{\text{Halo}}/M_\odot) \geq 14.0$ haloes.

2.3. Initial Selection of Massive Galaxies

We begin by making an initial selection of massive galaxies with reliable redshift from the HSC survey. The goal is to have a parent sample that contains a reasonably complete sample of $\log(M_*/M_\odot) \geq 11.5$ galaxies at $0.3 < z < 0.5$. According to Leauthaud et al. (2016), such galaxies should have $i_{\text{SDSS,cModel}} \leq 21.0$ mag. Therefore, we first select all galaxies with $i_{\text{HSC,cModel}} \leq 21.5$ ⁶ in regions that are covered by all five bands, and have reached the expected depth of WIDE survey. The HSC cModel photometry is similar to the SDSS cModel algorithm. It fits the flux distribution of an object using a combination of de Vaucouleur and exponential components after the PSF convolution is considered. For more details about the algorithm, please see Bosch et al. in prep.; and its performance has been tested using synthetic objects (Huang et al. in prep.). Although the overall performance of HSC cModel photometry is accurate down to very faint magnitude, it tends to underestimate the total flux of massive ETGs (will discuss this in details later). This is partially caused by issues with deblending process (see more discussion in Bosch et al. in prep.), but also reflects the intrinsic limitation of cModel, as the real flux distributions of massive galaxies are often too extended to be modeled this way at the depth of HSC images. For this reason, we will perform careful photometric measurements to derive more accurate total luminosity and stellar mass, and the sample selected here serves as an initial one for us to work on.

⁵See: <http://risa.stanford.edu/redmapper/>

⁶Difference of response curves between SDSS i and HSC i filter is tiny

We select objects that are classified as galaxies, have well defined centroids, are deblended successfully, and have cModel magnitudes in all five bands. After a few more quality control criteria (saturation, cosmic-ray, optical artifact) are applied⁷, we select 1760845 galaxies in this sample that will be referred as `hscPho`.

As reliable photometric redshift using HSC photometry is still a working progress, we only use objects with either spectroscopic redshift or robust red-sequence photo-z from the `redMaPPer` catalog. We first match the `hscPho` sample with the external spec-z catalog compiled by HSC database⁸ with a $1.0''$ radius, and it leads to 116813 matched objects, and 42696 objects are at $0.3 \leq z \leq 0.5$. Most of these redshifts come from either SDSS/BOSS or GAMA survey. For objects without external spec-z, we also match the sample with the `redMaPPer` catalog, and add objects with useful red-sequence photo-z (z_λ) back in. Together, this gives us a sample of bright galaxies with useful redshift.

2.4. Massive Central Galaxies from Low and High Mass Halos

Based on recent constraints of M_* - M_{Halo} relation (e.g. Leauthaud et al. 2012, Behroozi et al. 2013, Kravtsov et al. 2014), massive galaxies with $\log(M_*/M_\odot) > 11.5$ are hosted by dark matter halos with a large range of mass. Although we can not measure halo mass for individual galaxy, we can still broadly separate them into galaxies in small groups ($\log(M_{\text{Halo}}/M_\odot) < 14.0$) and large groups/clusters ($\log(M_{\text{Halo}}/M_\odot) > 14.0$), and investigate their stellar mass distributions.

We first match the initial sample of massive galaxies with the central galaxies in `redMaPPer` catalog with $1.0''$ radius, which results in 375 matched ones at $0.3 \leq z \leq 0.5$. We will refer this sample of **central galaxies in** $\log(M_{\text{Halo}}/M_\odot) \geq 14.0$ **halos** as `redBCG` in this work. A small fraction of `redMaPPer` centrals within HSC footprints do not have matched object due to severe contamination from optical artifacts. Spec-z is not available for 67 (17.9%) of the sample, but their z_λ should be very accurate (median $|z_\lambda - z_{\text{Spec}}|$ is about 0.01 for the ones with spec-z). The median richness (λ) of these clusters is ~ 32 , corresponding to halo mass of $M_{200,c} \sim 1.7 \times 10^{14} h^{-1} M_\odot$. Given the uncertainty of richness estimate using shallow SDSS photometry, we mainly focus on the centrals of clusters that have $\lambda > 30$ ($M_{200,c} > 1.7 \times 10^{14} h^{-1} M_\odot$).

Then, we matched the initial sample with both the central and satellite galaxy catalogs of `redMaPPer` using a physical radius of 2.5 Mpc and absolute redshift difference of 0.05 (using z_λ for all members). By removing all the matched objects, we aggressively exclude galaxies that are associated with these massive halos. The rest 29973 galaxies should mostly live in $\log(M_{\text{Halo}}/M_\odot) < 14.0$ halos, and the real $\log(M_*/M_\odot) > 11.5$ ones among them should be dominated by central galaxies of these halos as the satellite contamination is very low at such high mass end (e.g. van Uitert et al. 2016). We will refer this sample of **central galaxies in** $\log(M_{\text{Halo}}/M_\odot) < 14.0$ **halos** as `nonBCG` later.

It is worth noting that, at $0.3 < z < 0.5$, most redshifts in both `redBCG` and `nonBCG` come from GAMA and SDSS/BOSS survey. The current sample partially overlaps with the GAMA

⁷each criterion affects less than 8% of the entire sample

⁸It is created by matching HSC objects with public data of several spectroscopic surveys (e.g. SDSS/BOSS; GAMA). Duplicated matches from different sources are merged through internal matching using $0.5''$ radius. For each object, the quality information of the spec-z from different catalogs are homogenized into a single flag that indicates whether the redshift is secure, and only secure spec-z are used in this work.

survey, which reaches to ~ 19.8 mag in r -band, and provides us unique spec-z for 14% of the entire initial sample. According to Taylor et al. (2011) (e.g. their Figure 6), at $z \sim 0.3$, the GAMA sample is 80% complete down to $10^{10.8} M_\odot$; but only 80% complete to $10^{12.0} M_\odot$ at $z \sim 0.5$. Meanwhile, the BOSS survey provides us the majority of spec-z in our samples. Due to the complex selection criteria for different subsamples within the BOSS survey (e.g. the LOWZ and CMASS), its M_* completeness is hard to estimate. Recently, through comparing with the Stripe 82 Massive Galaxy Catalog (S82-MGC; Bundy et al. 2015), Leauthaud et al. (2016) suggests that the BOSS spec-z is about 80% complete at $\log(M_*/M_\odot) \geq 11.6$ at $0.3 < z < 0.5$. Despite the difference in photometry and stellar mass estimates, we can expect our samples are reasonably complete above $\log(M_*/M_\odot) \geq 11.6$. We will further address the M_* completeness issue more carefully with the help of the photo-z from the S82-MGC sample (see Section 4.3).

3. MEASUREMENTS OF 1-D SURFACE BRIGHTNESS PROFILE

3.1. 1-D Surface Brightness Profile

To estimate the total luminosity of massive galaxies, and measure their one-dimensional stellar mass density profiles, we perform elliptical isophotes fitting using the IRAF task `Ellipse` (Jedrzejewski 1987). Compared to the popular two-dimensional model fitting method, the isophote fitting approach is much less sensitive to the choice of model type, number of components, and initial guesses of free parameters; is also less affected by the uncertainties of the sky background subtraction. This is particularly important for the massive ellipticals in our sample. The much deeper depth of the HSC images reveal much more extended structures, but also make it impossible and inappropriate to fit these galaxies with single Sérsic component as it often requires uncomfortably high Sérsic index (e.g. > 6.0), can not fit the center of massive galaxies well, and can not account for the radial variation of ellipticity and position angle. In principle, their surface brightness distributions can be described by models with multiple components (e.g. Huang et al. 2013b; Huang et al. 2013a). However, these models still suffer from issues like sensitivity to background subtraction, internal degeneracies of parameters, and choice of best number of components. Their robustness and physical meanings still deserve more investigations. Therefore, we think the 1-D method suits the scientific goal of this work better.

We first generate large cut-out images for galaxies in our samples, and make sure the image covers to at least 750 kpc from the center of the galaxy in radius, so we can safely assume that we cover the entire galaxy while still have enough space to estimate the background. We also reconstruct the PSF model using the central coordinate of the galaxy, and generate bad pixel mask. We choose i -band as the default band to extract 1-D surface brightness profile since it has the best seeing among all five bands, and can still serve as good stellar mass distribution tracer at $0.3 < z < 0.5$. Although z and Y-band should suffer less from potential internal dust extinction and radial variation of mass-to-light ratio, the sky background is much higher in these two bands, and the seeing conditions are often considerably worse than i -band.

Then we use a customized photometric procedures based

on SEP Python library to create object mask before we run `Ellipse`. The current HSC pipeline still has difficulties dealing with regions around bright galaxies as the extended wings from bright objects result in overestimated S/N that leads to “over-deblending” issue. Our customized pipeline is more flexible since we can run `SExtractor`-like measurements twice using different configurations for background subtraction, detection, and deblending. Global background, low-detection threshold, and conservative deblending help detects all the large, bright, or diffuse objects; while very small background box size and aggressive deblending together can help detect the faint objects that are on the extended envelope of bright galaxies or close to the galaxy center. The catalogs from these two steps are merged after the target galaxy at the center is identified and removed. To mask out most fluxes from other objects, we convolved the pixel segmentation of each object with a Gaussian kernel to increase its size. Then, these expanded pixel segmentations are merged with the bad pixel mask into a binary object mask. This method works very well for early-type galaxy that has smooth structural features.

Meanwhile, we also generate a mask of all objects detected by above procedures with a much more aggressive masking method (larger Gaussian kernel size). We treat the unmasked pixels as “sky pixels”, and rebin them using 6x6 box size. Then we use the median value of each box to generate the statistics of sky background. As expected, we often see negative median values in the distribution of sky pixels around our massive galaxies as the HSC pipeline tends to slightly over-subtract the background⁹. As this over-subtraction often leads to unphysical truncation of surface brightness profile, we provide an ad-hoc fix using a `SExtractor`-like background model created by SEP with 200x200 background box size. Such model can capture the overall negative sky value, modify the median sky pixel value very close to zero, and remove flux of nearby objects that are not perfectly masked out by our object mask.

Using the background-corrected cutout image and the mask, we run `Ellipse` based on strategy very similar to (Li et al. 2011). In summary, we start with `Ellipse` run with free central position and free geometry, then gradually constrain its behavior, and eventually extract 1-D surface brightness profile along the major photometric axis using isophotes with fixed center and shape. The 4th Fourier modes are included to fit the isophote better. In this way, we can extract the radial changes of the photometric “barycenter”, ellipticity, position angle, and overall isophotal shape (more “disky” or “boxy”, e.g. Kormendy et al. 2009) of these galaxies at the same time. At low surface brightness regime, the final profile can be sensitive to several configuration parameters of `Ellipse`. After some tests, we choose to use 0.1 dex in logarithm as the step in semi-major axis length between successive ellipses, and we use the median pixel value over the elliptical annulus after rejecting outlier pixels twice with 3σ -clipping. These parameters are selected to make the final profile less affected by any nearby objects, and please see Appendix B for more details about the extraction of 1-D profile. Fig. 5 shows one example of the 1-D measurement, where we also compare the profile of the galaxy with the PSF profile extracted using circular aperture.

It is worth noting that, can not extract reliable 1-D profiles

⁹This is similar to what happened to SDSS as shown in Blanton et al. 2011, but at a lesser level. The sky background of each CCD is modeled using a Chebyshev-polynomial fit to the pixels that do not belong to any object after they are smoothed

¹⁰<http://www.sos.siena.edu/jmoustakas/isedfit/>

¹¹<http://scholar.harvard.edu/cconroy/sps-models>

for a small fraction of massive galaxies in both samples due to masked-out center that is caused by either physical (e.g. late-stage major merger) or unphysical (e.g. nearby foreground galaxy or bright star) reasons. For the physically interacting ones, it might be worth studying whether their profiles are different with the relaxed ones, but we have to rely on 2-D decomposition technique for that.

We correct the surface brightness profiles for Galactic extinction and cosmological dimming, and then integrate them to a series of radii to get the luminosity within different physical apertures. Although the 1-D profile from our *i*-band image can reach to as deep as 30 mag arcsec⁻², we often see sudden truncation or large fluctuation of profiles at the very low surface brightness part due to uncertainty from background subtraction or contamination from other objects. Therefore, we only consider the profiles above 28.5 mag arcsec⁻² reliable in this work. Using this conservative estimate, we can reliably estimate total luminosity within ~ 120 kpc aperture, which is enough for this work.

We also apply the isophotes derived on *i*-band images to other bands in “force-photometry” mode `Ellipse` run to get rough estimates of color profiles. Without taking the difference in seeing and background into account, these color profiles can not be used for physical discussion. But with the help of *K*-correction from the next section, we show that there is no systematic difference in color gradient between redBCG and nonBCG sample.

4. STELLAR MASSES AND STELLAR MASS DENSITY PROFILES

4.1. Stellar Masses from SED Fitting

As mentioned earlier, we estimate the total stellar mass and the stellar mass density profiles by applying the average M_*/L_* of the galaxy to the 1-D luminosity profiles we just extracted. We use the broadband Spectral Energy Distributions (SEDs) fitting (see Walcher et al. 2011 for a recent review) code `iSEDFit`¹⁰ (¹¹) to estimate the average M_*/L_* and *k*-corrections using five band `cModel` photometry. The `cModel` photometry not only takes the PSF convolution into account, but also fixes the model parameters of both de Vaucouleur and exponential components to the ones from a reference filter (mostly *i* band) except for their amplitudes. Therefore, it provides accurate *average* color of the galaxy despite it tends to underestimate the total flux (e.g. Huang et al. in prep.).

`iSEDFit` takes a simplified Bayesian approach. In short, it first generates a large grid of SEDs from synthetic stellar population models by drawing randomly from the prior distributions of relevant parameters (e.g. age, metallicity, dust extinction, and star formation history). Based on these models, it uses the observed photometry and redshift to compute the statistical likelihood, and generate the posterior probability distribution (PDF) functions of each parameter. To get the best estimate of certain parameter, `iSEDFit` “integrates” the full PDF over all the other “nuisance” parameters. Then, the median value of the resulting marginalized PDF is used as the best value, while the $1-\sigma$ uncertainty is derived from the cumulative PDF. Please refer to ? for technical details and performance of `iSEDFit`.

In this work, we derive average M_*/L_* using the Flexible

Stellar Population Synthesis¹¹ (FSPS; v2 . 4; Conroy & Gunn 2010a, Conroy & Gunn 2010b) model based on the MILES¹² (Sánchez-Blázquez et al. 2006, Falcón-Barroso et al. 2011) stellar library and Chabrier (2003) IMF between 0.1 to 100 M_{\odot} . We use the delayed- τ model with stochastic star burst as the form of star formation history (SFH), and choose a set of reasonable parameters after some tests. Such form of SFH is appropriate for massive quiescent galaxies at low redshift (e.g. Kauffmann et al. 2003). For stellar metallicity, we assume flat distribution between 0.004 to 0.03 (which is the highest metallicity allowed by FSPS models). And, the Calzetti et al. (2000) extinction law is adopted with a order two Gamma distribution of A_V between 0 to 2 magnitude. And, since most galaxies in both samples are red, quiescent galaxies, the results are not very sensitive to parameters related to SFH and internal dust extinction. To achieve reasonably good sampling across these parameters, we generate 250000 models.

We construct five band SED using cModel magnitude corrected for the Galactic extinction. As for the photometric error, the current cModel photometry underestimates the flux errors of these massive galaxies as it only includes statistical error, not the systematic uncertainties from the model-fitting procedure. From tests using synthetic objects, we find that the average accuracy of cModel photometry at bright end is hardly better than 1% when the systematic uncertainties are included. Therefore, we supply iSEDFit with simplified flux errors assuming $S/N = 100$ for riz bands, and $S/N = 80$ for gY bands (that typically have shallower depth and higher background noise). Given such assumption, the typical uncertainty of $\log(M_{\star}/M_{\odot})$ for both samples is around 0.08 to 0.10 dex at the high- M_{\star} end. Please see Appendix. B for more details about the discussion of the SED fitting results. In Fig. 3, we show an example of SED fitting result. [Song: Not sure if we need to show one example, but put one here for now.]

4.2. Comparison with S82-MGC

Given the heterogeneous redshift resources of both samples, we further investigate the M_{\star} completeness issue by comparing with galaxies in the common regions with the S82-MGC sample. The S82-MGC sample matches the deeper SDSS photometric data in the Stripe 82 region (Annis et al. 2014) with the near infrared data from the United Kingdom Infrared Telescope Infrared Deep Sky Survey (UKIDSS; Lawrence et al. 2007). With the help of deeper photometry and accurate photo-z, the S82-MGC sample is complete to $\log(M_{\star}/M_{\odot}) \geq 11.2$ at $z < 0.7$, making it perfect sample to verify the completeness of our samples.

We match the hscPho sample with S82-MGC, and get 20453 common galaxies at $0.3 < z < 0.5$ (referred as s82Pho sample). We estimate their stellar mass using cModel SED in exactly the same way, and the M_{\star} from HSC shows good correlation with the S82-MGC SED (five optical bands from SDSS and NIR data from UKIDSS) fitting M_{\star} (S82-MGC also used iSEDFit, with slightly different priors). Then we estimate the volume densities distributions of galaxies in redBCG, nonBCG, and s82Pho samples (Fig. 4) using rough values of the survey areas they occupied (as we only care about the relative shapes of the density distributions). The distribution of nonBCG sample starts to deviates from the s82Pho one below $\log(M_{\star}/M_{\odot}) < 11.6$, indicating that the sample starts to become incomplete within $0.3 < z < 0.5$. As for

the redBCG sample, their mass completeness should be better thanks to the reliable z_{λ} from redMaPPer catalog; and its log-normal behaviour is consistent with the mass function of galaxies located in a narrow halo mass bin (REF). After accounting for the correction for total luminosity, this suggests that at least the nonBCG sample is not perfectly complete below $\log(M_{\star}/M_{\odot}) < 11.7$. This is most likely due to the incompleteness of the BOSS spec-z sample. Although it is unlikely that such incompleteness will bias the results of our comparisons, we will bear this in mind, and match the two samples carefully in $\log(M_{\star}/M_{\odot})$ and redshift space before comparing them.

4.3. Stellar Mass Corrected for Total Luminosity

Using the best-fit stellar mass from iSEDFit (referred as $M_{\star,\text{cModel}}$), we estimate the average M_{\star}/L_{\star} in i -band, then use that M_{\star}/L_{\star} to convert the 1-D luminosity density profiles into stellar mass density profiles; and also convert the luminosity within 10 and 100 kpc apertures into corresponding stellar mass estimates (referred as $M_{\star,10\text{kpc}}$ and $M_{\star,100\text{kpc}}$). From now, we use $M_{\star,100\text{kpc}}$ as the new proxy of “total” stellar mass of these galaxies. And we also derive the k -corrected luminosity and colors from the results. In Appendix. B, we also show the outputs like the average stellar age, metallicity, and internal dust extinction all behave reasonably for both samples, but will not use them for further scientific analysis.

As expected, the integration of 1-D profile out to very large radius help recover more luminosity (stellar mass) compared to the cModel results. We highlight this in the left panel of Fig. 5 as we show the distributions of differences between $M_{\star,100\text{kpc}}$ and $M_{\star,\text{cModel}}$, and their relations to the $M_{\star,100\text{kpc}}$. For both samples, we see the “extra mass” recovered by 1-D photometry increases with $M_{\star,100\text{kpc}}$, therefore this improvement impacts the redBCG sample more. This is basically consistent with the fact that the structure of massive ETGs depends on its stellar mass in a way that more massive ones tends to be more extended (e.g. REF). Apparently, such mass-dependent difference between $M_{\star,100\text{kpc}}$ and $M_{\star,\text{cModel}}$ will result in difference of the SMF. As the slope and normalization of SMF at high mass end is very sensitive to both cosmology and interesting baryonic processes such as AGN feedback (REF), they are particularly important in constraining the galaxy evolution model, and therefore became the center of some intense arguments (REF). Although the jury is still out on this topic, it has become clear that popular results using SDSS photometry (REF) underestimate the total luminosity (stellar mass) of massive ETGs. However, past works (e.g. REF) often relied on either stacking of shallow images or the extrapolation of models to investigate this effect. Using the deep HSC images, we have the potential to answer this question much better. Detailed studies of SMF deserves more careful investigations of many systematic issues (e.g. REF), so we just show the impact of the “extra mass” on the volume density distributions of both samples (Fig. 5, right panel). Generally speaking, the stellar mass corrected for total luminosity shifts the distribution toward the higher mass end, and slightly modify the slope. People who want to use HSC photometry or other cModel-like photometry to study the properties and evolution of SMF should be aware of such effect.

As mentioned earlier, our assumption of using an average M_{\star}/L_{\star} ignores its radial variation. It is well known that mas-

¹¹<http://www.iac.es/proyecto/miles/pages/stellar-libraries/miles-library.php>

sive ETGs have negative optical color gradient which indicates a gradient of M_*/L_* (e.g. La Barbera et al. 2012; D’Souza et al. 2015), but the gradient is smooth and shallow out to a few times of the effective radius (color gradient at the very outskirt is still not well quantified). And, for the comparison between the redBCG and nonBCG samples, Our results should remain intact as long as there is no significant differences of color gradient between these two samples. We will discuss this more later, but initial results do suggest a smooth color gradient out to very large radius, and there is no systematic difference in color gradients of the two samples. Both suggest that the average M_*/L_* approach should work reasonably well for our goals. And, we should mention that our approach is in principle very similar to the method adopted by the GAMA survey (Taylor et al. 2011), where the average M_*/L_* comes from SED fitting of PSF-matched aperture photometry while the more accurate total luminosity relies on multi-band Sérsic model fitting (Kelvin et al. 2012).

TODO: Since we put 1-D profile in front of this section, we need to have a summary of the final samples, as a fraction of them does not have 1-D profile.

In Fig. 5, we show the $M_{*,100\text{kpc}}$ -color relations using both k -corrected $g-r$ and $g-z$ colors for redBCG and nonBCG samples. Both samples follow the same tight red-sequence without much contamination from the ‘‘blue cloud’’. At fixed $M_{*,100\text{kpc}}$, not apparent offset is seen in the distributions of optical colors between the two samples, which suggests both samples come from old, quiescent galaxies with similar stellar population. This is also consistent with the work that found the average stellar population of massive central galaxy does not depends on halo mass (e.g. Park et al. 2007). To look into the potential environmental dependence of structure, we will focus on the mass range of $11.6 \leq M_{*,100\text{kpc}} \leq 11.9$, where both samples should have reasonable completeness, and the mass distributions of the two samples overlap the most. Within this $M_{*,100\text{kpc}}$ range, the redBCG and nonBCG samples still show difference in their redshift distributions. We will address this before we compare their average stellar mass density profiles.

5. RESULTS

5.1. M_* -Size Relations

As most of the past works on the environmental dependence of structures for massive galaxies often focus on the scaling relation between stellar mass and effective radius (or half-light radius, e.g. REF), we first show similar relations for both redBCG and nonBCG samples (Fig. 8, upper panel), and compare them with the relation for central galaxies in Huertas-Company et al. 2013 (HC13) at $z < 0.09$, also with the relation from van der Wel et al. 2014 (vdW14) for ETGs at $z \sim 0.25$ using HST.

Since we do not perform model fitting, the half-light radius (R_{50}) is defined as the radius along the major axis that encloses 50% of luminosity within 100 kpc, and is derived using the luminosity curve-of-growth. In principle, the 1-D estimate of R_{50} is uncertain due to PSF smearing effect and the choice of maximum luminosity radius. In cases of the very massive ETGs in our samples, their R_{50} are large enough to avoid the influence of PSF; and, as the luminosity profiles at 100 kpc already reach to very low surface brightness, the R_{50} is quite stable using slightly

different definition of maximum luminosity (we explored luminosity within 120, 150 kpc, and within the maximum radius of the profiles, the results are the same). At the same time, comparing with R_e extracted from 2-D models, the 1-D R_{50} has the advantage of being less sensitive to the background subtraction uncertainty, and independent of the choice of model.

Both HC13 and vdW14 estimate R_e using 2-D single-Sérsic model fitting to SDSS and HST images; and their stellar masses are derived from SED fitting using BC03 (Bruzual & Charlot 2003) synthetic population model. vdW14 assumed the same Chabrier IMF while HC13 used the Kroupa IMF. We empirically correct the systematic caused by different IMF choices by applying a -0.03 dex shift. As shown in Appendix. B, we noticed an average 0.1 dex decrease of stellar mass when using BC03 model instead of the FSPS one, therefore, we also increase the stellar masses in HC13 and vdW14 accordingly. Despite these differences, the mass-size relations for both redBCG and nonBCG follow the relation from HC13 with a very similar slope. The relation from vdW14 shows a clear offset that could be caused by systematics in measurements of both stellar mass and effective radius, The important point is that, just like many previous results, the central galaxies from lower- and higher-mass halos seem to follow very similar mass-size relation¹³. This seems to reinforce the view that, at low redshift, environment plays a marginal (if there is any) role in determining the structure of massive galaxies.

However, as we mentioned in the introduction, the lack of difference on the mass-size relation could be caused by (1) insufficient depth of the image; (2) that effective radius is a biased parameter that can not reflect the subtle environmental dependence. The deep HSC images should solve problem (1), but we still need to rule out the second possibility by looking into more structural details.

5.2. Comparison of Surface Mass Density Profiles

5.2.1. Internal Comparison and Comparison with Previous Works

Compared to the scaling relations, the stellar mass density profiles contain more useful structural details that can help us diagnose the environmental effect. Before the actual comparisons, we first show the general properties of these 1-D profiles by separating both samples into different bins of $M_{*,100\text{kpc}}$ and redshift, also by comparing them with results from literature (Fig. 9). For profiles in each bin, we derive the median profile along with its uncertainty using bootstrap resampling method (5000 times). The left panel of Fig. 9 focuses on different mass bins. As expected, for both samples, higher $M_{*,100\text{kpc}}$ moves the median mass density profile upward a little in the inner region, but makes it more extended in the outer part. In the mass range we explored ($\geq 10^{11.2} M_\odot$), most of these ETGs are slow-rotating (e.g. Cappellari et al. 2013) giant ellipticals with boxy inner isophotal shape (e.g. Kormendy et al. 2009), and flattened density profile at the center (e.g. Lauer et al. 2007), but their structure in the outskirt clearly does NOT response to stellar mass increase in a self-similar way.

In principle, this is consistent with result from HST observations of BCGs at $0.3 < z < 0.9$ (Bai et al. 2014) and the claimed positive correlation between luminosity and Sérsic index (e.g. Savorgnan et al. 2013)¹⁴; it is also consistent with the

¹³Limited by the narrow mass range and the small sample size of redBCG, we do not attempt to fit the relations

¹⁴But it does not mean such high Sérsic index model works well for massive ETGs as they fail at the inner-most region dramatically, and can not explain the radial variation of isophotal shape

picture that more massive ETGs experienced more recent (minor) mergers.

At the same time, such behaviour should make us very cautious about any indication of “environmental dependence of structure” as it may be degenerate with difference caused by stellar mass when the two samples are not perfectly matched in mass. This is exactly what we see in the median profiles of `redBCG` and `nonBCG` in the same mass bins. Although the comparison shows that `redBCG` shows much more extended outer envelope than `nonBCG`, the very similar profile in the inner ~ 10 kpc reveals that this is dominated by the different mass distributions in two samples.

In the middle panel of Fig. 9, we compare these median profiles with a few past works. (Huang et al. 2013b), derived the median stellar mass density profile for a small sample of very nearby ellipticals from the Carnegie-Irvine Galaxy Survey (CGS, Ho et al. 2011). Individual profile and total luminosity were derived from three-component 2-D models that describe both very inner and outer luminosity distributions of these galaxies accurately. The average stellar mass of this sample is around $10^{11.3} M_{\odot}$. Due to the proximity of this sample (< 100 Mpc), the average profile is unaffected by seeing within ~ 1 kpc. Most galaxies of the CGS sample are not in any cluster. The median profile qualitatively agrees with the median profile of `nonBCG` in the low mass bin, especially in the inner region. Outside the inner 15 kpc, the CGS median profile shows a slightly more prominent outer envelope. While this could simply reflect the small size of CGS sample (~ 30), interestingly, it is also consistent with the expectation if the mild mass growth from $z \sim 0.4$ mostly happened at the outskirt. The CGS images are already slightly deeper than SDSS images in r -band, however, the median profile can only reach to ~ 50 kpc (with much larger uncertainty compared to this work) for ETGs within ~ 100 Mpc. Such comparison clearly highlights the improvement made by the deep HSC images as individual profile of $z \sim 0.5$ galaxy is reliable out to at least 100 kpc.

At the similar redshift with our sample, we compare with mass density profile extracted from stacked images of massive ETGs at $0.25 < z < 0.50$ using HST/ACS images (Patel et al. 2013). These galaxies are selected at constant cumulative number density, and as progenitors of $z=0$ massive ETGs. The average stellar mass is $\sim 10^{11.2} M_{\odot}$ according to their estimates. However, given the shallower depth of the ACS images and the usage of the BC03 model (each could cause -0.1 dex mass offset compared to this work), this sample should be comparable to the `nonBCG` sample in the lowest mass bin, and the comparison of their median profiles does reflect that. Moreover, since the profile from HST/ACS image is not bothered by PSF within 1 Kpc, the comparison illustrates that the HSC median profiles in our redshift range are indeed not affected by seeing outside the shaded region. In fact, as we suggested, our estimate is quite conservative, the profiles within 5 kpc should be reliable.

Besides these observations, we also compare with the predicted average stellar mass density profile for central galaxies of massive halos ($13.5 < \log M_{200,c} < 14.0$) in simulation (Cooper et al. 2013). This is achieved by combining the detailed assembly information of halos from dark-matter-only simulation with semi-analytic model and particle-tagging technique (Cooper et al. 2010). Although the physical resolution and detailed baryonic processes are not as “realistic” as state-of-art hydro-simulation, it is very efficient in providing rough stellar mass distributions for large number of massive halos. Without

any adjustment, the profile is quite similar to the `nonBCG` sample in the $11.5 < \log M_{\star} < 11.7$ bin within inner 20 kpc; but it predicts a too significant outer envelope for its average halo mass. Without going into details to find the cause of such discrepancy in this work, the comparison already suggests that the comparison between deep observed mass density profiles with the ones from modern simulations is going to be quite interesting, especially in the outskirt.

The right panel of Fig. 9 focus on the impact of redshift distribution by grouping the $11.6 \leq \log M_{\star} < 11.9$ `redBCG` and `nonBCG` into two redshift bins. Under the same seeing condition, galaxy at higher redshift suffers more from PSF smearing effect in the central region; and the cosmological dimming of surface brightness also makes the outer region more difficult to measure. As shown here, although the median profiles of the same sample in two redshift bins follow each other very well at the outer part, they start to differ in the central region as the one from higher redshift bin ends up with a more flattened profile compared to the one for lower redshift bin. In the same redshift bin, median profiles of `redBCG` and `nonBCG` are very similar in the region affected by seeing. Therefore, when comparing structures of massive galaxies using ground-base images, it is also important to make sure different samples share similar redshift distributions.

5.2.2. Matched Samples Using M_{\star} from the GAMA survey

As the sky coverage of this release greatly overlaps with the GAMA survey, we start the detailed comparison with an external check using the stellar mass estimated by (Taylor et al. 2011). The purpose is still to investigate the impact of deeper photometry on the analysis of structure of massive galaxies. The stellar masses of GAMA galaxies are initially derived through careful optical-SED fitting (BC03 model; Chabrier IMF) using the PSF-matched aperture photometry. Then they were corrected for the total luminosity estimated using single-Sérsic 2-D model to multi-band images (Kelvin et al. 2012). We separate the `redBCG` and `nonBCG` galaxies that also have spec-z and stellar mass in GAMA DR2 (Liske et al. 2015). Most of galaxies in these subsamples have $z < 0.40$.

To compare the median mass density profiles of these two subsamples, we need to make sure that they share as similar as possible distributions in at least stellar mass ($M_{\star,GAMA}$) and redshift. To achieve this, we match the `redBCG` sample that always has smaller size to the `nonBCG` galaxies by searching for the N nearest neighbours on the $M_{\star,GAMA}$ - z plane using the KDTree algorithm provided by `scikit-learn` Python package (Pedregosa et al. 2011). As we only keep unique `nonBCG` galaxy in the matched sample, we manually adjust the value of N to achieve the most similar distribution. In case that the distribution of mass or redshift for `redBCG` is bi-modal, we also try to split the sample into two, and match them separately. Normally N is between 3 to 8.

In Fig. 10, we show the results of matches for subsamples using $M_{\star,GAMA}$. To increase the number of available `redBCG` to match, we loosen its selection criteria to $\lambda \geq 20$ and $P_{CEN} \geq 0.6$. Based on the distributions of the two samples at the $M_{\star,GAMA}$ - z plane, and their overlapped region, we match them in two bins of $M_{\star,GAMA}$ that have slightly different redshift ranges. Besides the 2-D distributions, we also use the histograms and kernel density distributions (KDE) of mass and redshift, along with their median values and interquartile ranges to evaluate the similarity between the samples. For stellar mass, its KDE is gen-

erated using a Gaussian kernel with width equals to the typical uncertainty of the mass estimate (0.06-0.10); and for redshift, we choose 0.025 as the width of the Gaussian kernel. For the samples in two $M_{*,\text{GAMA}}$, the matches appear to be very good. We also check the distributions of k -corrected optical colors of the two samples, just to confirm that their average colors are similar as while.

In Fig. 11, we show the individual profiles, median profiles along with their uncertainties derived using 5000 times bootstrap resampling, and the relative difference between the profile of the `redBCG` and `nonBCG` subsamples. It is very clear that, for both mass bins, the `redBCG` has a much more extended outer envelope, while its profile inside ~ 10 kpc is very close to the `nonBCG` one. This is inconsistent with the matched distributions of their “total” stellar mass, and reveals potential issue with the stellar mass estimated by GAMA. We can reproduce very similar results using the luminosity density profiles (with or without k -correction) of these matched samples, which suggests that the main problem does not lie in the estimate of M_*/L_* , but in the measurement of total luminosity using single-Sérsic model.

This highlights the importance of deep optical images in studying the structure of massive galaxies.

As both estimates of $M_{*,\text{GAMA}}$ and λ can have noticeable uncertainty, the sizes of both samples are quite small, and the distributions of individual profile in two samples overlap even in the outskirt, we also perform a simple statistical test to prove the significance of the differences between the profiles. Assuming that there are N_r `redBCG` and N_h `nonBCG`, we put these two samples together, and randomly draw N_r galaxies with putting-back from the mixed sample; then we compute the difference between the median profile of the random sample and the one for original `nonBCG` sample; repeat this procedure 2000 times so that it can provide us the statistical distribution of the difference. In cases of these $M_{*,\text{GAMA}}$ -matched samples, the differences of median profiles are very robust.

5.2.3. Matched Samples Using $M_{*,100\text{kpc}}$

Finally, we....

5.2.4. Matched Samples Using $M_{*,10\text{kpc}}$

5.3. Relations between stellar mass within different physical apertures

6. DISCUSSION

6.1. The Impact of M/L Gradient

6.2. Ellipticity Profiles

6.3. Massive Satellites of the $\lambda > 20$ Haloes

[Song: TBD:optional]

6.4. Implications on Assembly History of Massive Galaxies

Comparison of mass profiles with previous studies at high redshift

6.5. M_* and Structural Evolution between $0.3 < z < 0.5$

6.6. Impact from “Fossil Galaxies”

“Fossil galaxy” is the most massive galaxy in a “fossil group/cluster” system. According to the commonly adopted definition, “fossil” systems are the group or cluster with high X-ray luminosity and large magnitude gap between the two

brightest galaxies (REF: Ponman1994; Jones2003). Both observations and simulations suggest that they could represent the final stage of the hierarchical merging process in a group/cluster mass halo that is formed at very early epoch (e.g. REF: Khosroshahi2004, 2007; DOnghia2005; Dariush2007). Under this interpretation, at fixed halo mass, the central galaxy of a fossil system typically has larger stellar mass than the one in normal system (e.g. Harrison2012), as it has “consumed” most satellites early on; However, the “low richness” of a fossil system makes it difficult for red-sequence finder like `redMaPPer` to reliably identify (e.g. Figure 17 of Sadibekova2014). If some massive ETGs in our `nonBCG` sample are actual the centrals galaxies of fossil clusters, it could bias our conclusions about the relation between structure and “environment”.

Although it is possible that fossil systems formed earlier than normal clusters, the difference in detailed merging history is still unclear, hence it is hard to imagine the structural differences between fossil central galaxies and regular BCGs with same M_* . Naively speaking, more frequent mergers for fossil centrals should result in more extended stellar envelope. However, the distributions of epoch and mass-ratio of those mergers also matter.

The lack of any difference in stellar population properties may suggest It is still not clear how the mass assembly history of fossil central

6.7. Potential Impact from the Intra-Cluster/Group Light

As the `redBCG` sample moves into the galaxy cluster regime in term of halo mass, it is inevitable to discuss the impact of the (in)famous intra-cluster light component to our results.

7. SUMMARY AND FUTURE PLANS

With the help of the high quality, deep optical images provided by the HSC survey,

7.1. Future improvements

1. Improvements of HSC data reduction: better sky modeling; `redMaPPer` clusters using HSC photometry.
2. Comparison with 2-D image modeling method.
3. “Correct” the PSF smearing effect at the center with the help of residual correct 2-D model.

The Hyper Suprime-Cam (HSC) collaboration includes the astronomical communities of Japan and Taiwan, and Princeton University. The HSC instrumentation and software were developed by the National Astronomical Observatory of Japan (NAOJ), the Kavli Institute for the Physics and Mathematics of the Universe (Kavli IPMU), the University of Tokyo, the High Energy Accelerator Research Organization (KEK), the Academia Sinica Institute for Astronomy and Astrophysics in Taiwan (ASIAA), and Princeton University. Funding was contributed by the FIRST program from Japanese Cabinet Office, the Ministry of Education, Culture, Sports, Science and Technology (MEXT), the Japan Society for the Promotion of Science (JSPS), Japan Science and Technology Agency (JST), the Toray Science Foundation, NAOJ, Kavli IPMU, KEK, ASIAA, and Princeton University.

Funding for SDSS-III has been provided by the Alfred P. Sloan Foundation, the Participating Institutions, the National Science Foundation, and the U.S. Department of Energy. The

SDSS-III web site is <http://www.sdss3.org>. SDSS-III is managed by the Astrophysical Research Consortium for the Participating Institutions of the SDSS-III Collaboration including the University of Arizona, the Brazilian Participation Group, Brookhaven National Laboratory, University of Cambridge, University of Florida, the French Participation Group, the German Participation Group, the Instituto de Astrofísica de Canarias, the Michigan State/Notre Dame/JINA Participation Group, Johns Hopkins University, Lawrence Berkeley National Laboratory, Max Planck Institute for Astrophysics, New Mexico State University, New York University, Ohio State University, Pennsylvania State University, University of Portsmouth, Princeton University, the Spanish Participation Group, University of Tokyo, University of Utah, Vanderbilt University, Uni-

versity of Virginia, University of Washington, and Yale University.

TODO: Full acknowledgement

- [Acknowledgements for Kevin and Alexie's funding](#)

- [Acknowledgements for the Python libraries](#)

This research made use of [Astropy](#), a community-developed core Python package for Astronomy ([Astropy Collaboration et al. 2013](#)); [scikit-learn](#), a machine-learning library in Python ([Pedregosa et al. 2011](#)) [sep](#) Source Extraction and Photometry in Python ([Barbary et al. 2015](#)).

REFERENCES

- Alam, S., Albareti, F. D., Allende Prieto, C., et al. 2015, *ApJS*, 219, 12
 Annis, J., Soares-Santos, M., Strauss, M. A., et al. 2014, *ApJ*, 794, 120
 Astropy Collaboration, Robitaille, T. P., Tollerud, E. J., et al. 2013, *A&A*, 558, A33
 Axelrod, T., Kantor, J., Lupton, R. H., & Pierfederici, F. 2010, in Proc. SPIE, Vol. 7740, Software and Cyberinfrastructure for Astronomy, 774015
 Bai, L., Yee, H. K. C., Yan, R., et al. 2014, *ApJ*, 789, 134
 Barbary, Boone, & Deil. 2015, sep: v0.3.0
 Behroozi, P. S., Wechsler, R. H., & Conroy, C. 2013, *ApJ*, 770, 57
 Bellstedt, S., Lidman, C., Muzzin, A., et al. 2016, *MNRAS*, 460, 2862
 Bernardi, M., Meert, A., Sheth, R. K., et al. 2016a, ArXiv e-prints
 —. 2016b, *MNRAS*, 455, 4122
 —. 2013, *MNRAS*, 436, 697
 Blanton, M. R., Kazin, E., Muna, D., Weaver, B. A., & Price-Whelan, A. 2011, *AJ*, 142, 31
 Bruzual, G., & Charlot, S. 2003, *MNRAS*, 344, 1000
 Bundy, K., Leauthaud, A., Saito, S., et al. 2015, *ApJS*, 221, 15
 Calzetti, D., Armus, L., Bohlin, R. C., et al. 2000, *ApJ*, 533, 682
 Cappellari, M., McDermid, R. M., Alatalo, K., et al. 2012, *Nature*, 484, 485
 —. 2013, *MNRAS*, 432, 1862
 Chabrier, G. 2003, *PASP*, 115, 763
 Conroy, C., & Gunn, J. E. 2010a, FSPS: Flexible Stellar Population Synthesis, Astrophysics Source Code Library
 —. 2010b, *ApJ*, 712, 833
 Conroy, C., & van Dokkum, P. G. 2012, *ApJ*, 760, 71
 Cooper, A. P., D'Souza, R., Kauffmann, G., et al. 2013, *MNRAS*, 434, 3348
 Cooper, A. P., Cole, S., Frenk, C. S., et al. 2010, *MNRAS*, 406, 744
 Driver, S. P., Hill, D. T., Kelvin, L. S., et al. 2011, *MNRAS*, 413, 971
 D'Souza, R., Vegetti, S., & Kauffmann, G. 2015, *MNRAS*, 454, 4027
 Eisenstein, D. J., Weinberg, D. H., Agol, E., et al. 2011, *AJ*, 142, 72
 Falcón-Barroso, J., Sánchez-Blázquez, P., Vazdekis, A., et al. 2011, *A&A*, 532, A95
 Farahi, A., Evrard, A. E., Rozo, E., Rykoff, E. S., & Wechsler, R. H. 2016, *MNRAS*, 460, 3900
 Ho, L. C., Li, Z.-Y., Barth, A. J., Seigar, M. S., & Peng, C. Y. 2011, *ApJS*, 197, 21
 Huang, S., Ho, L. C., Peng, C. Y., Li, Z.-Y., & Barth, A. J. 2013a, *ApJ*, 768, L28
 —. 2013b, *ApJ*, 766, 47
 Huertas-Company, M., Shankar, F., Mei, S., et al. 2013, *ApJ*, 779, 29
 Inagaki, T., Lin, Y.-T., Huang, H.-J., Hsieh, B.-C., & Sugiyama, N. 2015, *MNRAS*, 446, 1107
 Ivezić, Z., Tyson, J. A., Abel, B., et al. 2008, ArXiv e-prints
 Kauffmann, G., Heckman, T. M., White, S. D. M., et al. 2003, *MNRAS*, 341, 54
 Kelvin, L. S., Driver, S. P., Robotham, A. S. G., et al. 2012, *MNRAS*, 421, 1007
 Kormendy, J., Fisher, D. B., Cornell, M. E., & Bender, R. 2009, *ApJS*, 182, 216
 Kravtsov, A., Vikhlinin, A., & Meshcheryakov, A. 2014, ArXiv e-prints
 La Barbera, F., Ferreras, I., de Carvalho, R. R., et al. 2012, *MNRAS*, 426, 2300
 Lauer, T. R., Gebhardt, K., Faber, S. M., et al. 2007, *ApJ*, 664, 226
 Lawrence, A., Warren, S. J., Almaini, O., et al. 2007, *MNRAS*, 379, 1599
 Leauthaud, A., Tinker, J., Bundy, K., et al. 2012, *ApJ*, 744, 159
 Leauthaud, A., Bundy, K., Saito, S., et al. 2016, *MNRAS*, 457, 4021
 Li, Z.-Y., Ho, L. C., Barth, A. J., & Peng, C. Y. 2011, *ApJS*, 197, 22
 Liske, J., Baldry, I. K., Driver, S. P., et al. 2015, *MNRAS*, 452, 2087
 Lupton, R., Blanton, M. R., Fekete, G., et al. 2004, *PASP*, 116, 133
 Magnier, E. A., Schlaflay, E., Finkbeiner, D., et al. 2013, *ApJS*, 205, 20
 Meert, A., Vikram, V., & Bernardi, M. 2015, *MNRAS*, 446, 3943
 Miyazaki, S., Komiyama, Y., Nakaya, H., et al. 2012, in Proc. SPIE, Vol. 8446, Ground-based and Airborne Instrumentation for Astronomy IV, 84460Z
 Oke, J. B., & Gunn, J. E. 1983, *ApJ*, 266, 713
 Park, C., Choi, Y.-Y., Vogeley, M. S., et al. 2007, *ApJ*, 658, 898
 Patel, S. G., van Dokkum, P. G., Franx, M., et al. 2013, *ApJ*, 766, 15
 Pedregosa, F., Varoquaux, G., Gramfort, A., et al. 2011, Journal of Machine Learning Research, 12, 2825
 Ricciardelli, E., Vazdekis, A., Cenarro, A. J., & Falcón-Barroso, J. 2012, *MNRAS*, 424, 172
 Rozo, E., & Rykoff, E. S. 2014, *ApJ*, 783, 80
 Rozo, E., Rykoff, E. S., Bartlett, J. G., & Melin, J.-B. 2015a, *MNRAS*, 450, 592
 Rozo, E., Rykoff, E. S., Becker, M., Reddick, R. M., & Wechsler, R. H. 2015b, *MNRAS*, 453, 38
 Rykoff, E. S., Rozo, E., Busha, M. T., et al. 2014, *ApJ*, 785, 104
 Salpeter, E. E. 1955, *ApJ*, 121, 161
 Sánchez-Blázquez, P., Peletier, R. F., Jiménez-Vicente, J., et al. 2006, *MNRAS*, 371, 703
 Saro, A., Bocquet, S., Rozo, E., et al. 2015, *MNRAS*, 454, 2305
 Savgornan, G., Graham, A. W., Marconi, A., et al. 2013, *MNRAS*, 434, 387
 Schlaflay, E. F., & Finkbeiner, D. P. 2011, *ApJ*, 737, 103
 Schlaflay, E. F., Finkbeiner, D. P., Jurić, M., et al. 2012, *ApJ*, 756, 158
 Simet, M., McClintock, T., Mandelbaum, R., et al. 2016, ArXiv e-prints
 Taylor, E. N., Hopkins, A. M., Baldry, I. K., et al. 2011, *MNRAS*, 418, 1587
 Tonry, J. L., Stubbs, C. W., Lykke, K. R., et al. 2012, *ApJ*, 750, 99
 van der Wel, A., Franx, M., van Dokkum, P. G., et al. 2014, *ApJ*, 788, 28
 van Uitert, E., Cacciato, M., Hoekstra, H., et al. 2016, *MNRAS*, 459, 3251
 Walcher, J., Groves, B., Budavári, T., & Dale, D. 2011, *Ap&SS*, 331, 1

APPENDIX

A. EXTRACTION OF 1-D SURFACE BRIGHTNESS PROFILE

B. DERIVE AVERAGE MASS-TO-LIGHT RATIO USING *ISEDFIT*

We adopt flat distribution between 0.5 to 14.0 Gyrs as prior for the look-back time when the star formation turned on. The exponential delayed time-scale (τ) is allowed to change between 0.1 to 3.0 with equal probability. The chance of random star burst is set at 0.2 for every 2 Gyrs. The duration of the star burst is drawn from a logarithmic distribution between 0.03 to 0.3 Gyr; and the mass fraction formed in the burst is from a logarithmic distribution between 0.01 and 1.0.

In principle, these choices of priors could leave systematic effects in the estimate of stellar mass (e.g. [Bernardi et al. 2016a](#)). For low- z massive ETGs like the ones in our sample, the details form of SFH, importance of random star burst, and the dust extinction should not be major concern. However, the choices of stellar population models and IMF can still change the results systematically. More discussions on this can be found in Appendix A. In short:

1. Both FSPS+MILES and BC03 (Bruzual & Charlot 2003) models still have difficulties recovering the optical color involving filters at the red end (e.g. $i-Y$), which could relate to the challenge for modern stellar population models to reproduce the optical color-color relation of red-sequence galaxies (e.g. Ricciardelli et al. 2012), or the shallower photometry of HSC-Y band data.
2. The BC03 provides slightly better overall χ^2 and systematically smaller M_* than the FSPS+MILES models. However, it is possible that the BC03 model tends to underestimate the M_*/L_* for a fraction of them as the estimate stellar age is unrealistically young for red, massive galaxies. Therefore, we still use the FSPS+MILES model as the fiducial one. But, switching to the BC03 model will not change any key result in this work.
3. The usage of Salpeter (1955) IMF results in systematically higher M_* (on average +0.25 dex of $\log(M_*/M_\odot)$). Although there are multiple lines of evidence that favor Salpeter or even more “bottom-heavy” IMF in the most massive ETGs (e.g. Conroy & van Dokkum 2012; Cappellari et al. 2012), we still present the main results using Chabrier IMF to accommodate galaxies with lower M_* in the sample, and to be as consistent as possible with a few other works. Also, the choice of IMF does not impact our results qualitatively.

Besides the priors for stellar population properties, different treatments of the light profile and accuracy of sky background subtraction are also important for the estimate of M_* as they strongly impact the estimate of total luminosity (e.g. Bernardi et al. 2013 and D’Souza et al. 2015). At the depth of SDSS, the default cModel photometry is already shown to be not very accurate at high- M_* end (e.g. Meert et al. 2015; Bernardi et al. 2016b) as it does not capture the extended envelope of these galaxies. As for HSC, it is much more challenging for cModel to recover the total luminosity of massive ETGs since the stellar envelope becomes even more extended for neither de Vaucouleur or exponential model to reproduce. However, the HSC cModel under the force-photometry mode can measure **average** color of the galaxy with great accuracy (e.g. Huang et al. in prep.), and provide us a reliable SED to estimate the **average** M_*/L_* . Considering this, we separate the process of estimating the total M_* of massive ETGs in our sample into two steps:

1. Firstly, using the redshift and cModel magnitude in five bands, we derive an initial estimate of the M_* of the galaxy. More importantly, we derive the **average** M_*/L_* in i -band of the galaxy, and use the best-fit SED to provide k -correction to the photometry.
2. In the next section, we will derive better estimate of total M_* using the more accurate total luminosity in i -band from integration of carefully measured 1-D surface brightness profile, and the average M_*/L_* from the SED fitting.

The basic results from iSEDfit are summarized in Figure 2, where we compare the relations between initial estimates of M_* and (both luminosity and star formation weighted) stellar age, metallicity, and dust extinction. As expected, most galaxies in our samples are $\log(M_{*,\text{ini}}/M_\odot) \geq 11.2$ massive galaxies that have old age, high metallicity ($1.5 \times Z_\odot$ is the highest metallicity allowed), and low dust extinction. Given that we only have photometry from five optical bands, degeneracies among age, metallicity, and dust extinction are naturally expected. We will not use them for any scientific reason in this work, but to show that they behave reasonably.

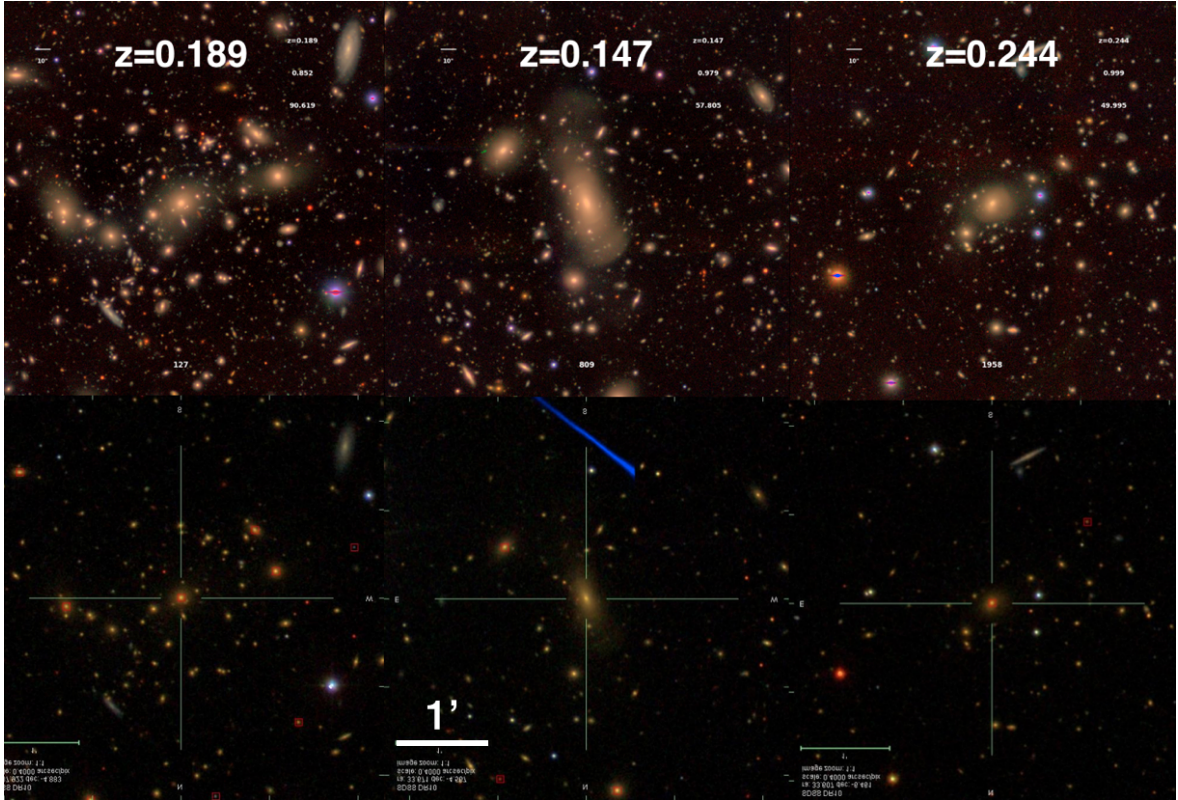


FIG. 1.— **TODO: Remake this figure:** Comparison of RGB 3-color images of nearby massive elliptical galaxies using SDSS and HSC images. The images are generated using *gri* band images according to the algorithm of (Lupton et al. 2004) with arcsinh stretch. It is clear that the depth of HSC image help map the stellar distributions out to much larger radius, and reveal more details in the outskirts compared to the SDSS ones.

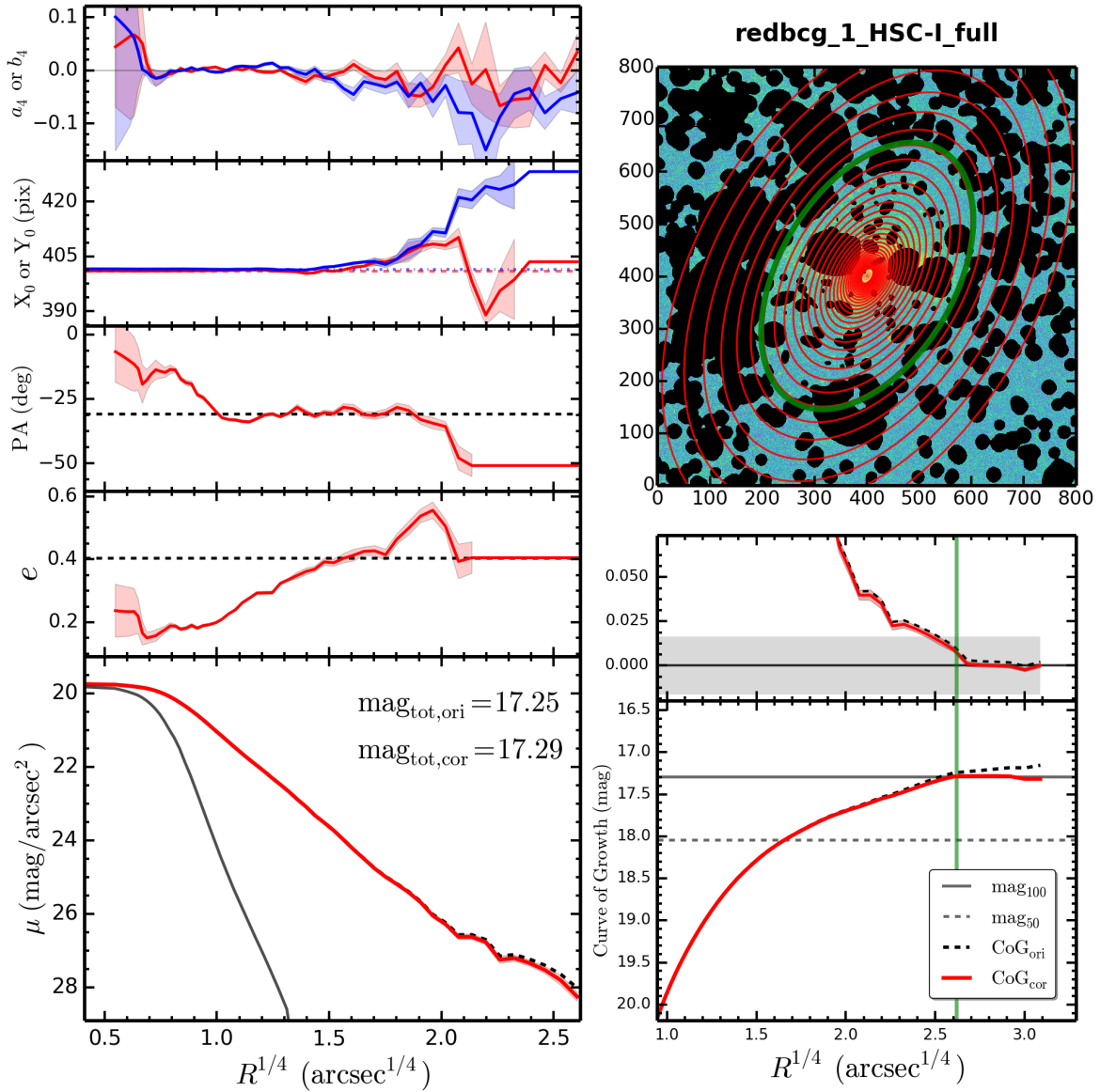


FIG. 2.— Figure.2TODO: Caption

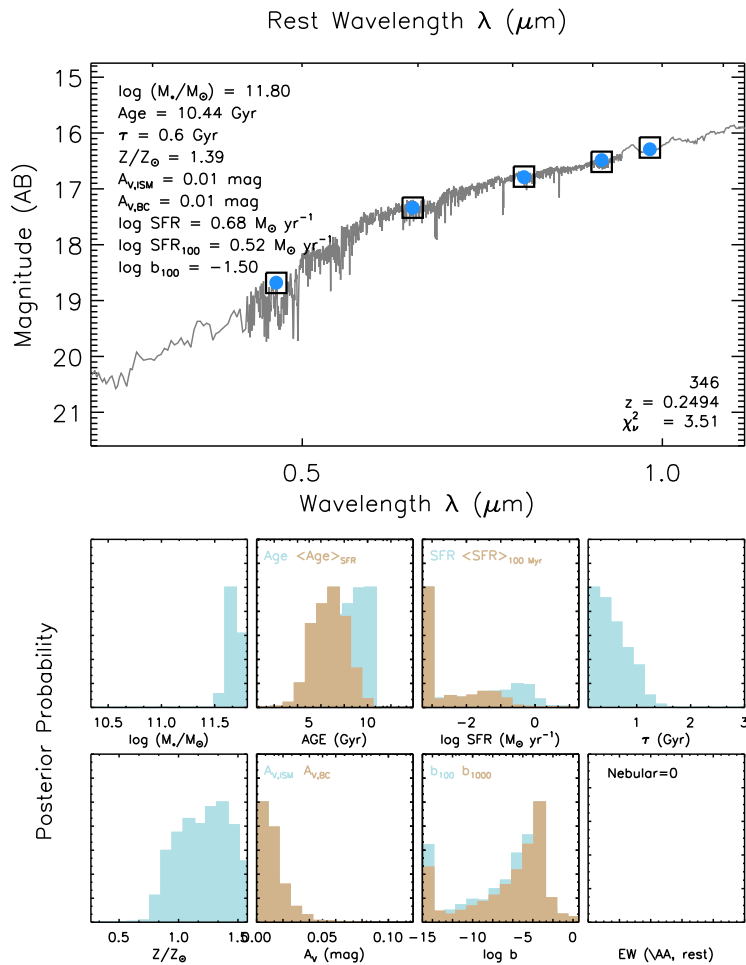


FIG. 3.— Figure 3 TODO: Caption

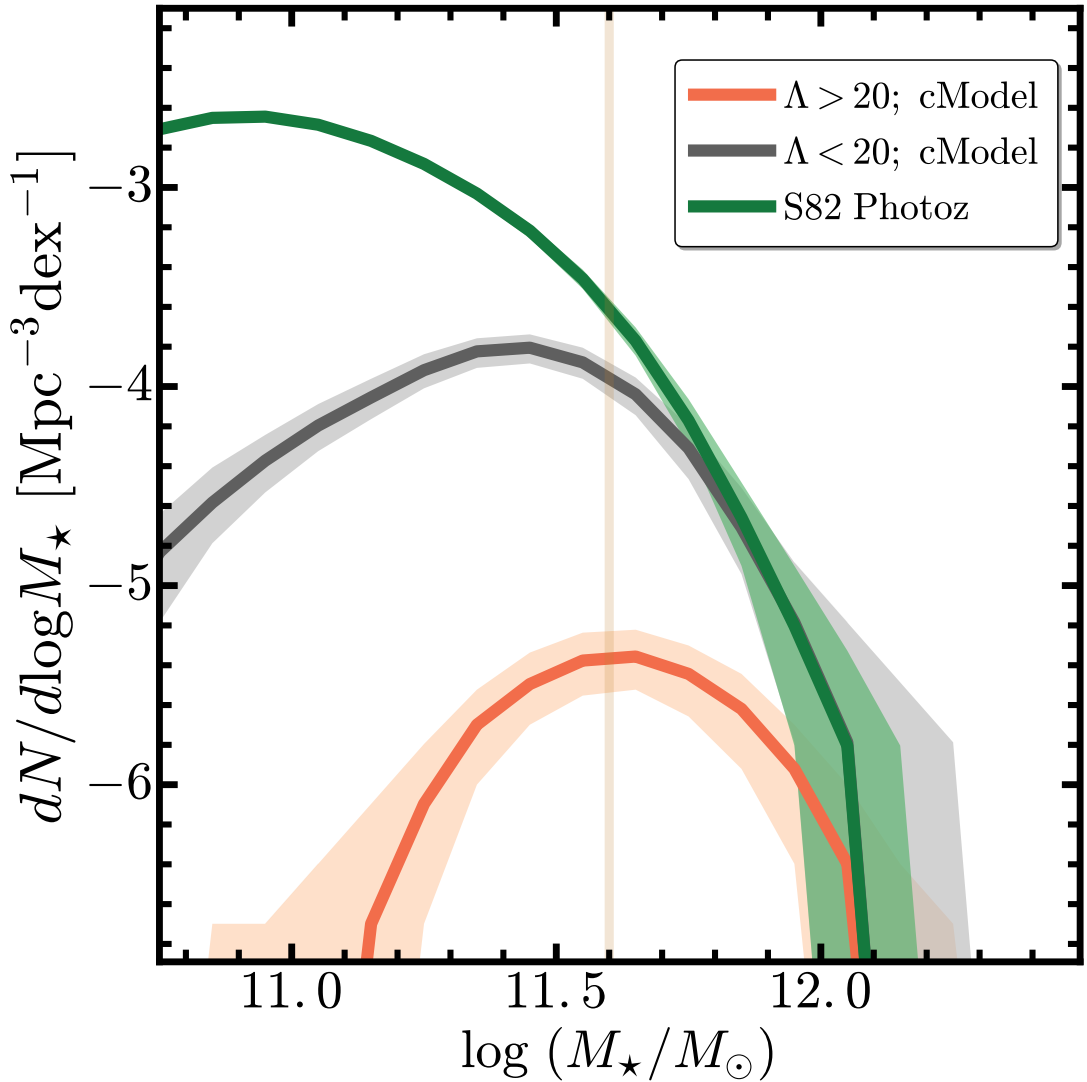


FIG. 4.— Figure.4**TODO: Caption**

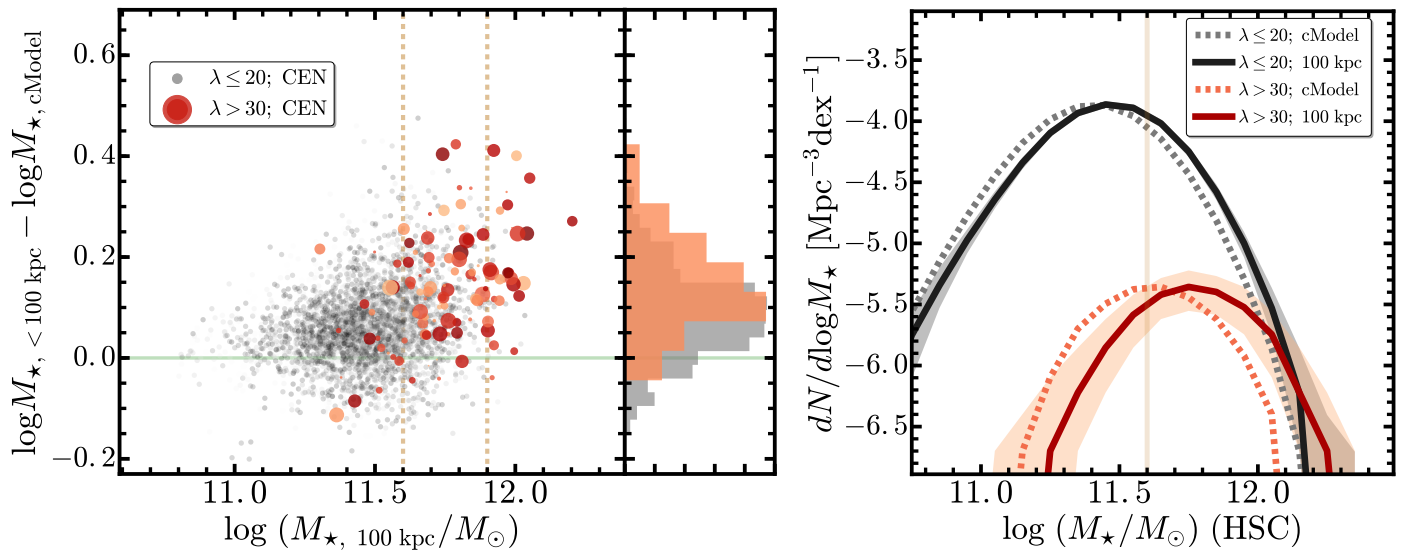


FIG. 5.— Figure 5 TODO: Caption

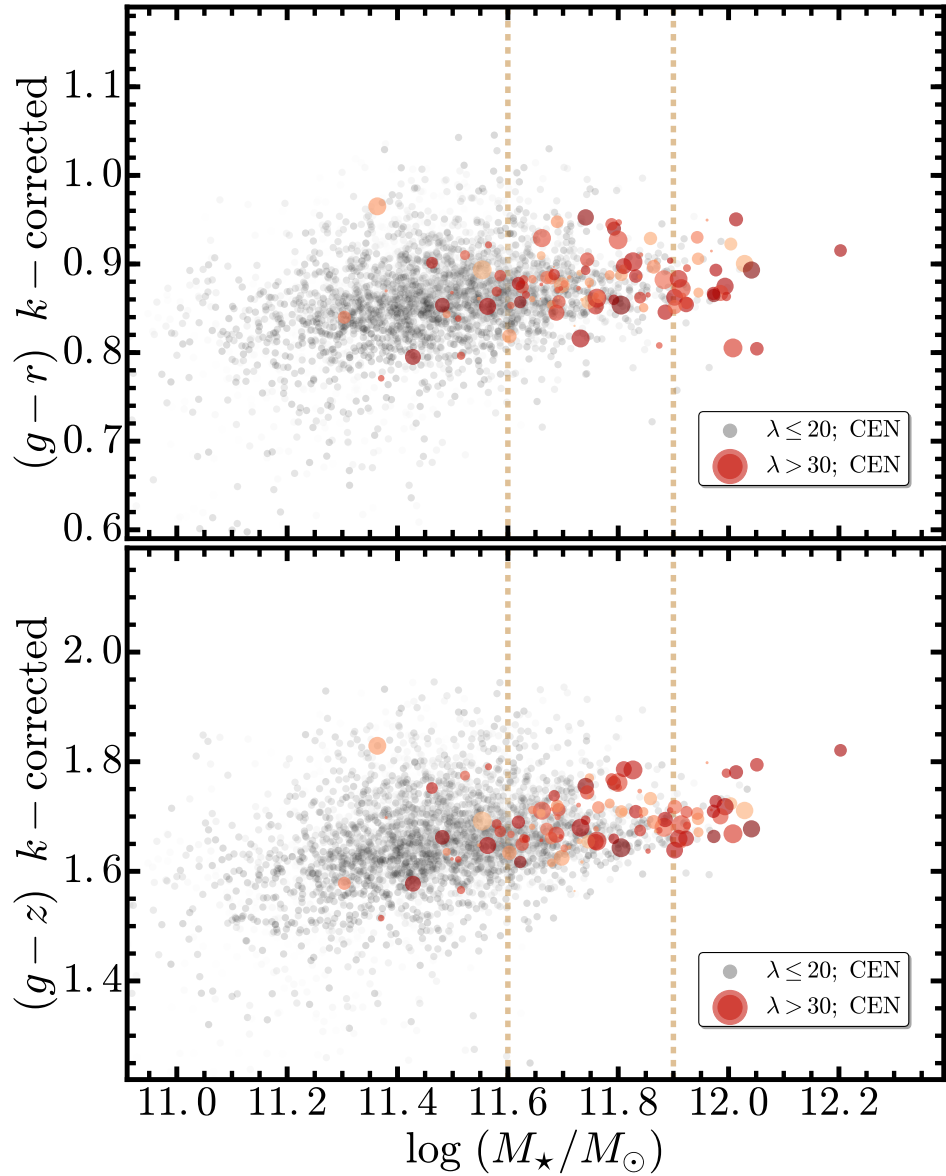


FIG. 6.— Figure.6TODO: Caption

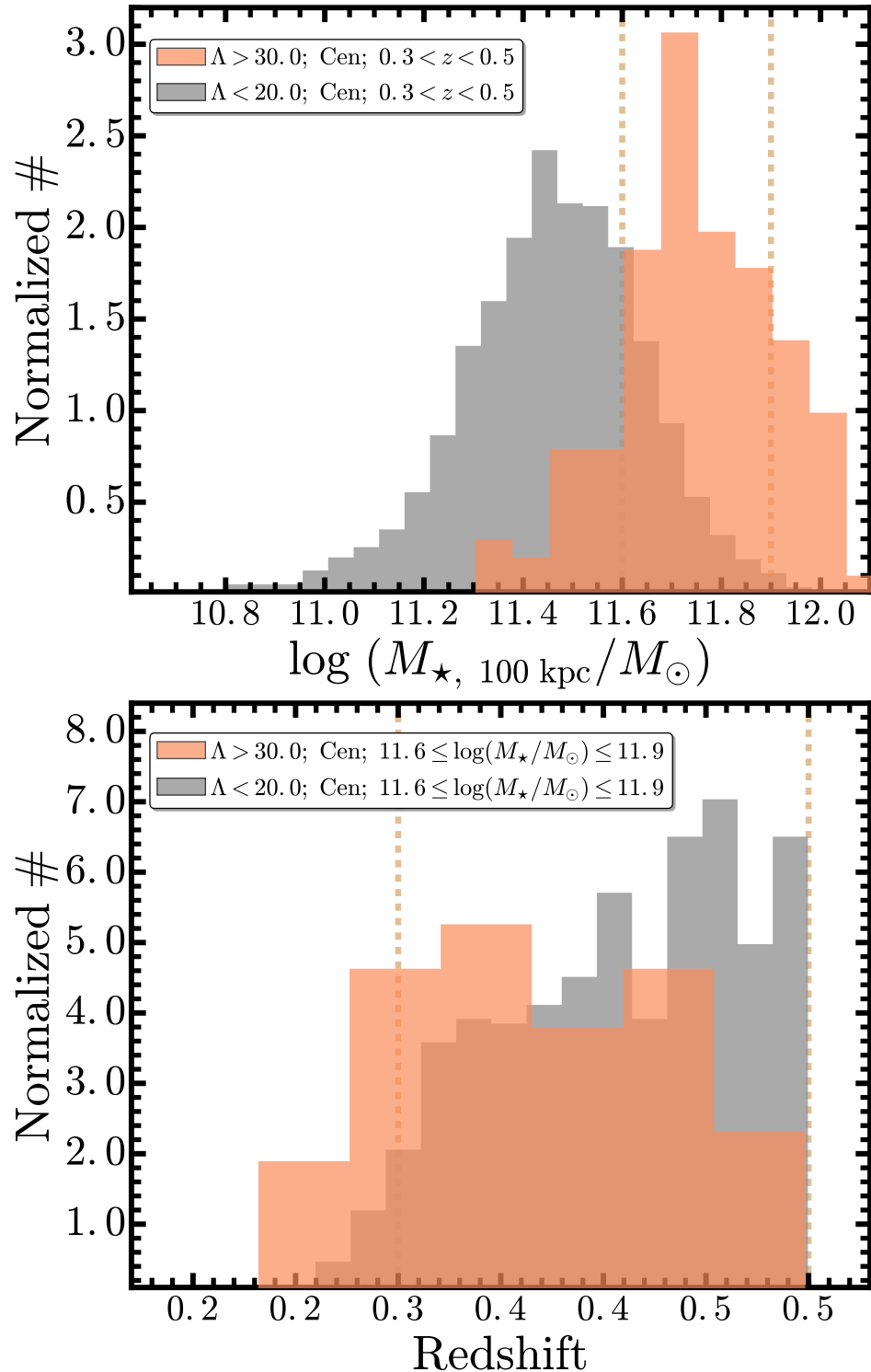


FIG. 7.— Figure.7 TODO: Caption

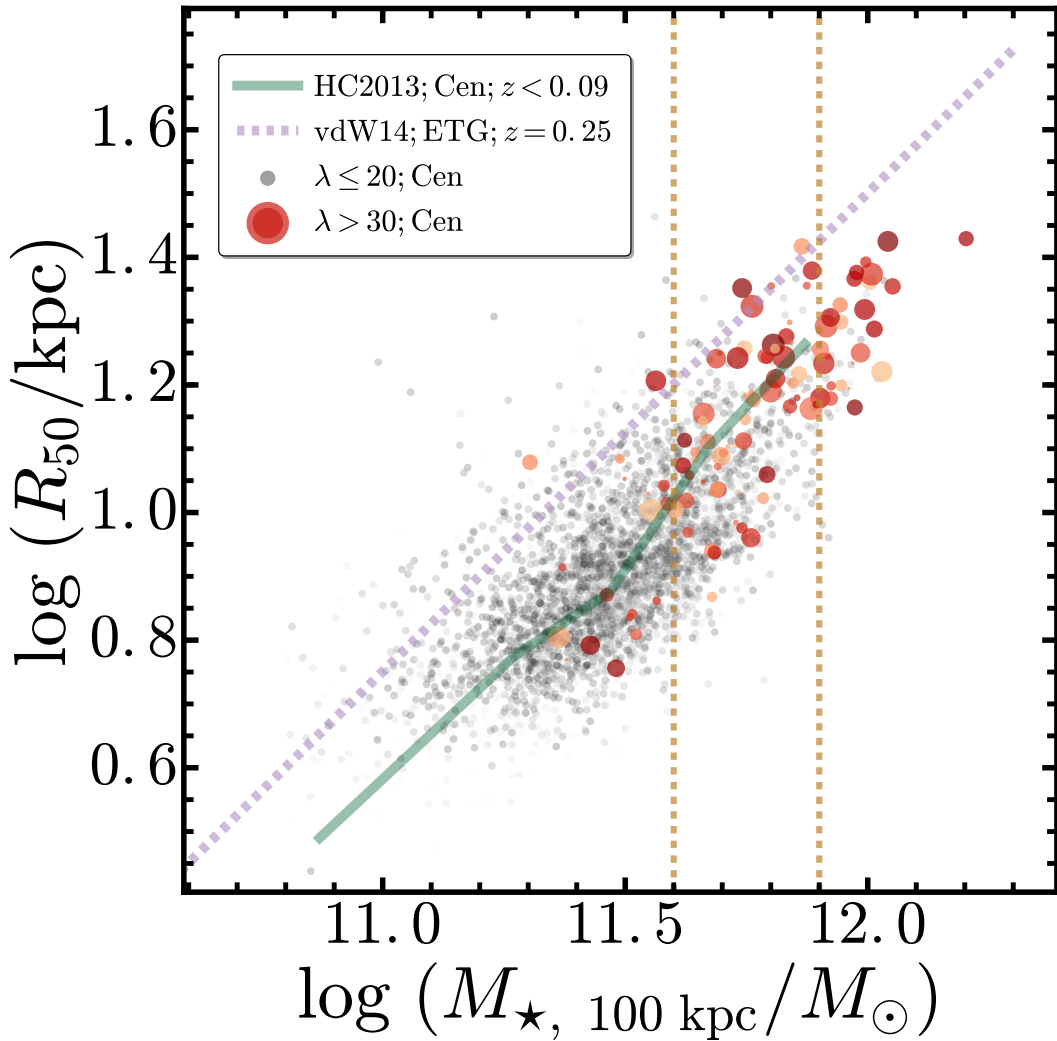


FIG. 8.— Figure.8TODO: Caption

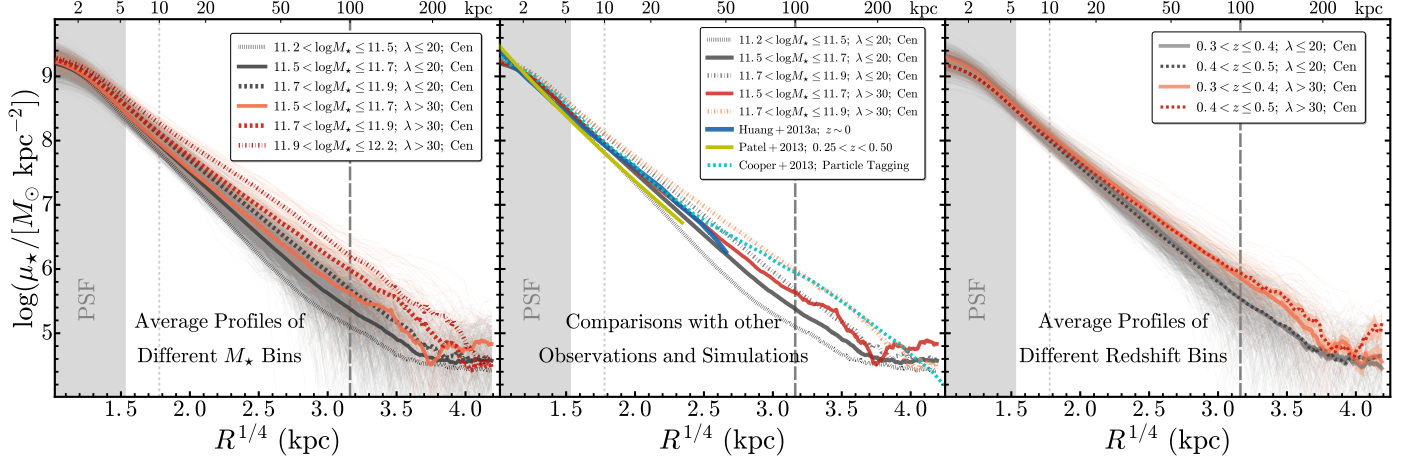


FIG. 9.— Figure 9 TODO: Caption

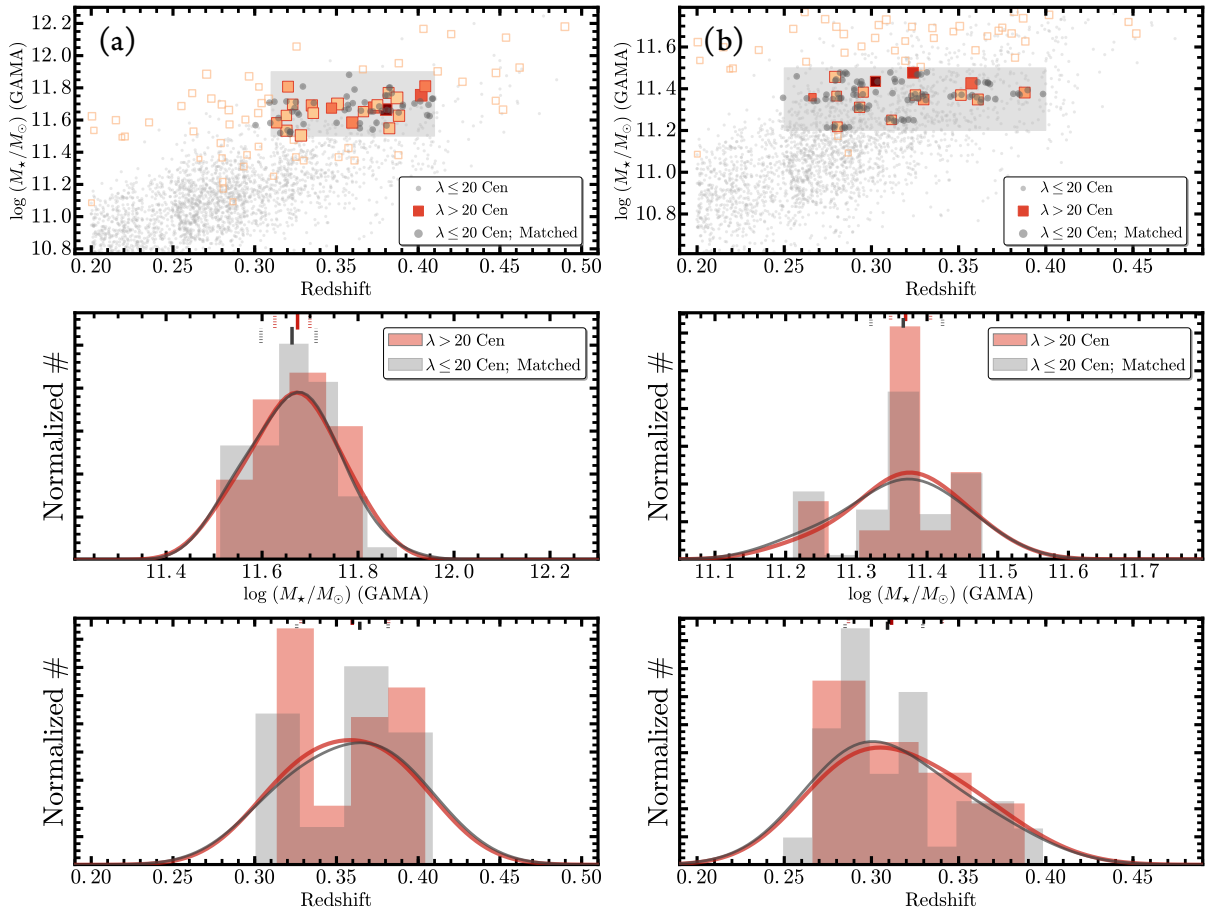


FIG. 10.— Figure 10 TODO: Caption

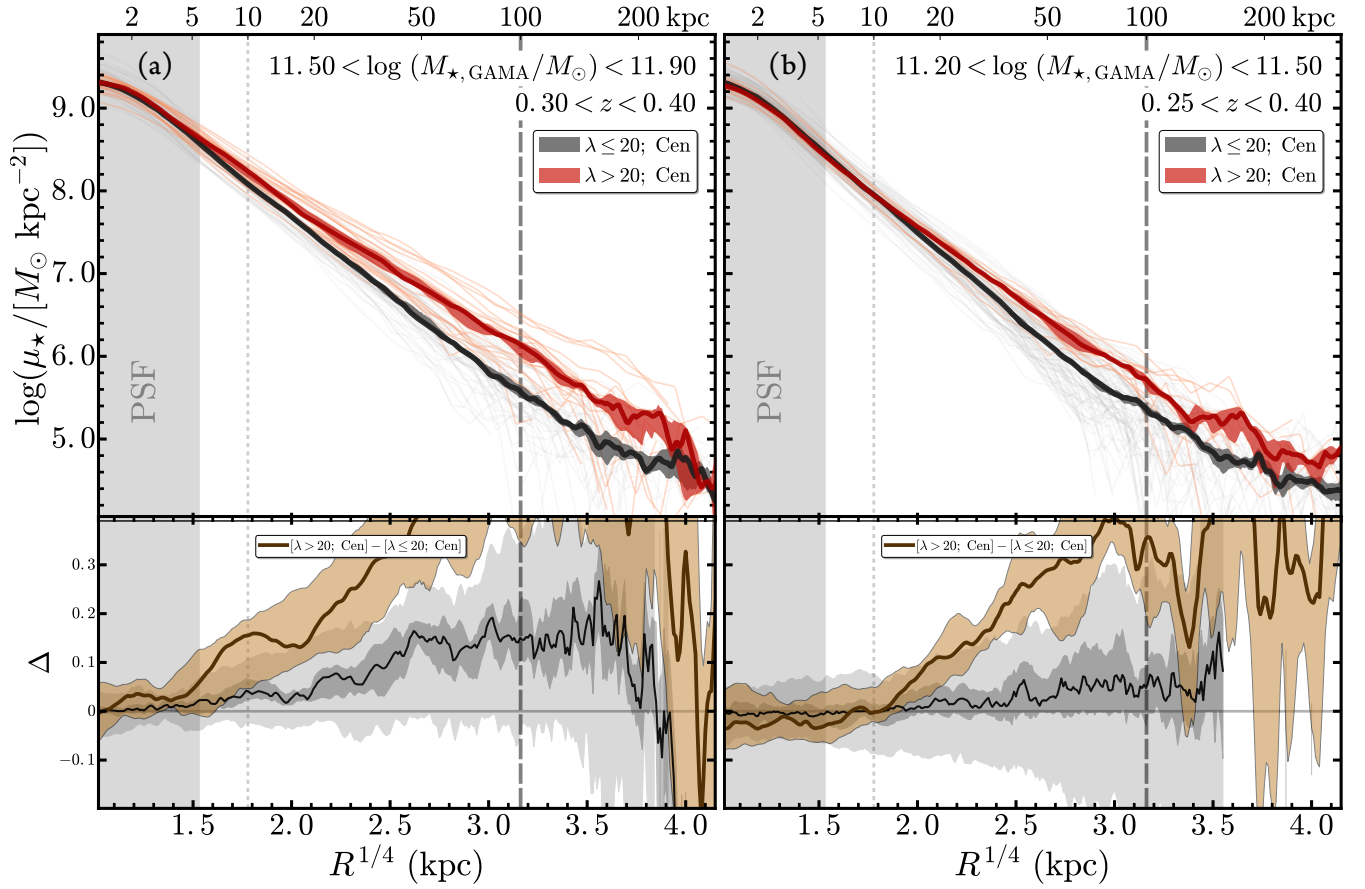


FIG. 11.— Figure.11 TODO: Caption

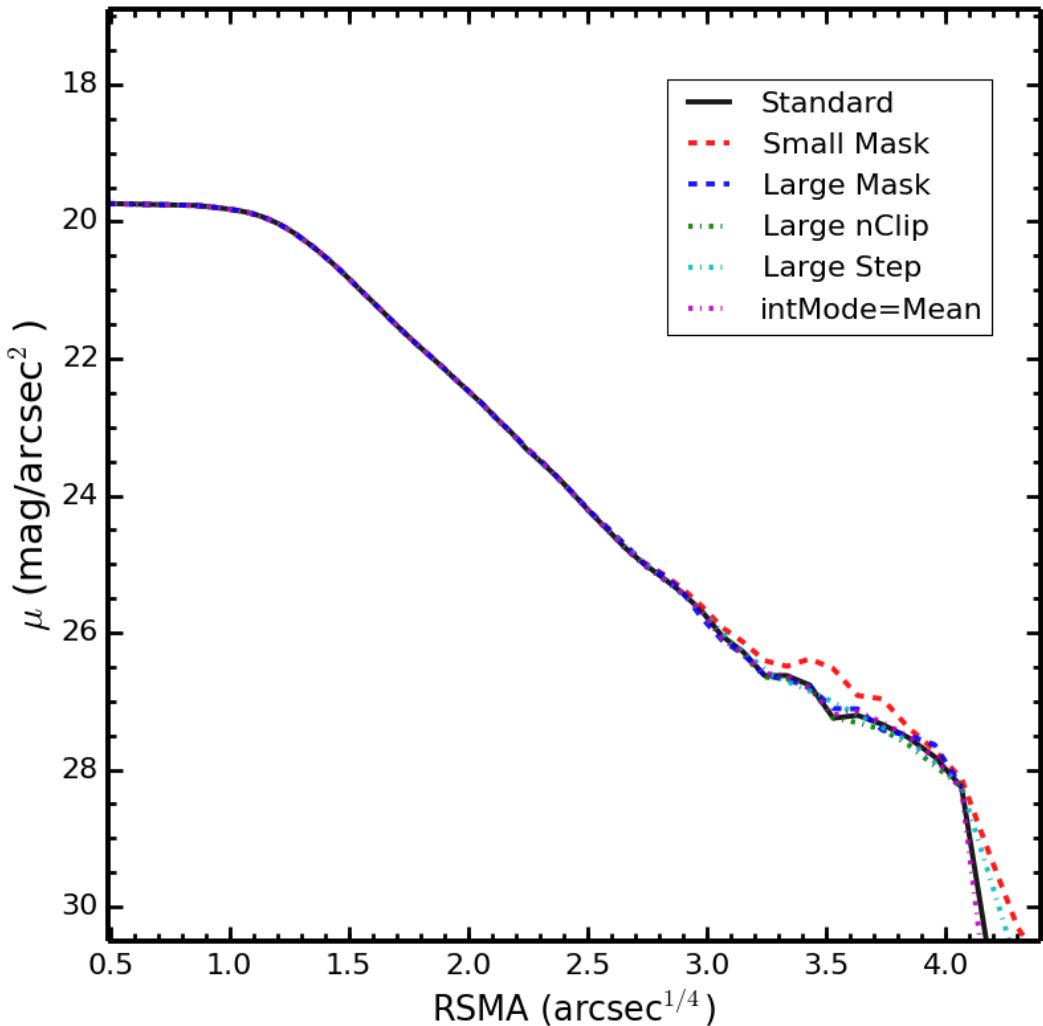
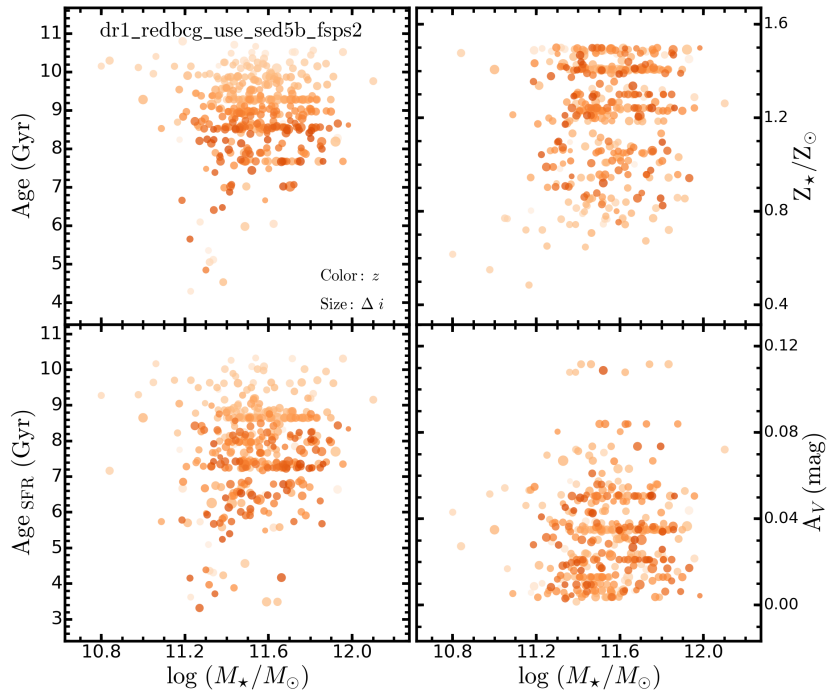
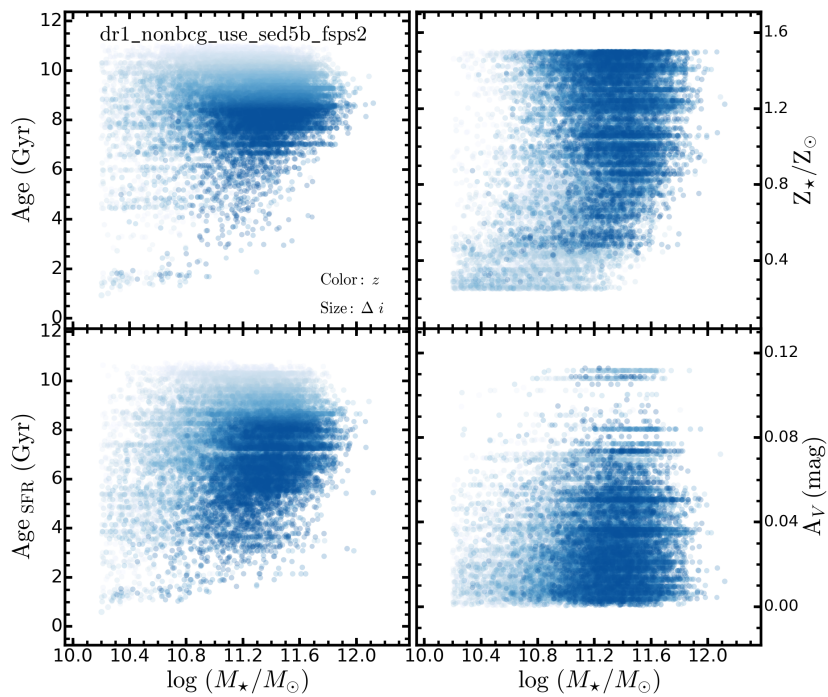


FIG. A1.— Figure.A1**TODO: Caption**

FIG. 2A.— Figure.2a**TODO: Caption**FIG. 2B.— Figure.2b**TODO: Caption**